



King's Research Portal

DOI:

[10.1038/ng.3558](https://doi.org/10.1038/ng.3558)

Document Version

Peer reviewed version

[Link to publication record in King's Research Portal](#)

Citation for published version (APA):

Toriyama, M., Lee, C., Taylor, S. P., Duran, I., Cohn, D. H., Bruel, A. L., Tabler, J. M., Drew, K., Kelly, M. R., Kim, S., Park, T. J., Braun, D., Pierquin, G., Biver, A., Wagner, K., Malfroot, A., Panigrahi, I., Franco, B., Al-lami, H. A., ... Wallingford, J. B. (2016). The ciliopathy-associated CPLANE proteins direct basal body recruitment of intraflagellar transport machinery. *Nature Genetics*, 48(6), 648-656. <https://doi.org/10.1038/ng.3558>

Citing this paper

Please note that where the full-text provided on King's Research Portal is the Author Accepted Manuscript or Post-Print version this may differ from the final Published version. If citing, it is advised that you check and use the publisher's definitive version for pagination, volume/issue, and date of publication details. And where the final published version is provided on the Research Portal, if citing you are again advised to check the publisher's website for any subsequent corrections.

General rights

Copyright and moral rights for the publications made accessible in the Research Portal are retained by the authors and/or other copyright owners and it is a condition of accessing publications that users recognize and abide by the legal requirements associated with these rights.

- Users may download and print one copy of any publication from the Research Portal for the purpose of private study or research.
- You may not further distribute the material or use it for any profit-making activity or commercial gain
- You may freely distribute the URL identifying the publication in the Research Portal

Take down policy

If you believe that this document breaches copyright please contact librarypure@kcl.ac.uk providing details, and we will remove access to the work immediately and investigate your claim.

The ciliopathy-associated CPLANE proteins direct basal body recruitment of intraflagellar transport machinery

Michinori Toriyama¹, Chanjae Lee¹, S. Paige Taylor², Ivan Duran², Daniel H. Cohn³, Ange-
Line Bruel⁴, Jacqueline M. Tabler¹, Kevin Drew¹, Marcus R. Kelley⁵, Sukyoung Kim¹, Tae
Joo Park^{1**}, Daniella Braun⁶, Ghislaine Pierquin⁷, Armand Biver⁸, Kerstin Wagner⁹, Anne
Malfrout¹⁰, Inusha Panigrahi¹¹, Brunella Franco^{12,13}, Hadeel Adel Al-lami¹⁴, Yvonne
Yeung¹⁴, Yeon Ja Choi¹⁵, University of Washington Center for Mendelian Genomics¹⁶,
Yannis Duffourd⁴, Laurence Faivre^{4,17}, Jean-Baptiste Rivière^{4,18}, Jiang Chen¹⁵, Karen J.
Liu¹⁴, Edward M. Marcotte¹, Friedhelm Hildebrandt⁶, Christel Thauvin-Robinet^{4,18}, Deborah
Krakow³, Peter K. Jackson⁵, and John B. Wallingford^{1*}

1. Dept. of Molecular Biosciences, University of Texas at Austin
2. Departments of Orthopaedic Surgery, Human Genetics and Obstetrics and Gynecology, David Geffen School of Medicine at UCLA, Los Angeles, California, USA
3. Department of Molecular Cell and Developmental Biology, University of California at Los Angeles, California, USA, 90095
4. EA4271 GAD Genetics of Developmental Anomalies, FHU-TRANSLAD, Medecine Faculty, Burgundy University, F-21079 Dijon, France
5. Stanford University School of Medicine, Baxter Laboratory, Department of Microbiology & Immunology, Stanford, California 94305
6. HHMI and Department of Medicine, Boston Children's Hospital, Harvard Medical School, Boston, MA 02115, USA
7. Clinical genetics centre, University Hospital Center, Liège, Belgian
8. Pediatric unit, Hospital Center, Luxemburg
9. Cardiological Pediatric unit, Hospital Center, Luxemburg
10. Clinic of Pediatric Respiratory Diseases, Infectious Diseases, Travel Clinic and Cystic Fibrosis Clinic at the Universitair Ziekenhuis UZ Brussel, Belgium
11. Department of Pediatrics Advanced, Pediatric Centre Pigmer, Chandigarh, India
12. Department of Medical Translational Sciences, Division of Pediatrics, Federico II University of Naples, Italy
13. Telethon Institute of Genetics and Medicine-TIGEM, Naples Italy
14. Dept. of Craniofacial and Stem Cell Biology, Dental Institute, King's College London
15. Departments of Pathology and Dermatology, Stony Brook University, Stony Brook, NY 11794
16. University of Washington Center for Mendelian Genomics; Full list of members available at: <http://www.mendelian.org/mendelian-center/university-of-washington>
17. Clinical genetics centre and Eastern referral centre for developmental anomalies and malformative syndromes, FHU-TRANSLAD, Children Hospital, CHU Dijon, F-21079 Dijon, France
18. Laboratory of Molecular Genetics, FHU-TRANSLAD, PTB, CHU Dijon, F-21079 Dijon, France

**Current Address: UNIST, Ulsan, Korea

*Corresponding author:

Patterson Labs
University of Texas
2401 Speedway
Austin, Tx. 78712
Wallingford@austin.utexas.edu
512-232-2784

65
66
67
68
69

Summary/Abstract:

70 Cilia use microtubule-based intraflagellar transport (IFT) to organize intercellular signaling.
71 The ciliopathies are a spectrum of human disease resulting from defects in cilia structure or
72 function. Mechanisms regulating assembly of ciliary multiprotein complexes and their
73 transport to the base of cilia remain largely unknown. Combine proteomics, *in vivo* imaging,
74 and genetic analysis of proteins linked to planar cell polarity (Inturned, Fuzzy, WDPCP), we
75 identified and characterized a new genetic module, which we term CPLANE (ciliogenesis,
76 and planar polarity effector) and an extensive associated protein network. CPLANE
77 proteins physically and functionally interact with the poorly understood ciliopathy protein Jbts17
78 at basal bodies, where they act to recruit a specific subset of IFT-A proteins. In the absence of
79 CPLANE, defective IFT-A particles enter the axoneme, and IFT-B trafficking is severely
80 perturbed. Accordingly, mutation of CPLANE genes elicits specific ciliopathy phenotypes in
81 mouse models and is associated with novel ciliopathies in human patients.

82
83
84
85
86

Introduction:

87 The ciliopathies are a broad class of human diseases that share an etiology of defective cilia
88 structure or function. These diseases span skeletal anomalies, craniofacial defects, cystic
89 kidneys, blindness, obesity, and other presentations, highlighting the wide array of physiological
90 functions that require components of the cilium^{1,2}.

91
92
93 Like all organelles, cilia are assembled and maintained by multi-protein machines. For example, the
94 BBSome is a large complex involved in trafficking of ciliary membrane proteins³; the Nphp and
95 Mks/B9 complexes assemble the ciliary transition zone, which controls access to the cilium^{4,5};
96 and dynein arms drive motile ciliary beating⁶. Likewise, the intraflagellar transport (IFT) system,
97 which links cargos to microtubule motors for transport into and out of cilia, is comprised of two
98 multi-protein complexes, IFT-A and IFT-B⁷⁻¹¹, IFT-A and IFT-B are frequently described as
99 controlling retrograde and anterograde traffic, respectively. However, both anterograde kinesin
100 motors and retrograde dynein motors can physically associate with IFT-A^{7,12-14}, and recent
101 studies highlight the role of IFT-A in ciliary entry and anterograde traffic^{15,16}. IFT-A and IFT-B are
102 each composed of a multi-protein “core” in addition to more loosely-bound “peripheral”
103 components^{15,17-19}.

104
105

106 While recent papers have begun to define the interactions between IFT complexes and their
107 cargoes (e.g. Ref. ^{20,21}), substantial questions remain concerning the mechanisms by which IFT
108 proteins are recruited to the base of cilia and assembled into IFT trains. Indeed, ciliopathies can
109 result from defects in cytosolic factors that facilitate dynein arm or BBSome transport and
110 assembly²²⁻²⁸, yet little is known about similar factors that may act on IFT. For example, basal
111 bodies in *Ttbk2* mutant mice fail to recruit certain subunits of the IFT-A and IFT-B complexes, but
112 they also fail to remove CP110, a key initial step for ciliogenesis²⁹. Likewise, *Odf1*, *Cep83/Ccdc41*,
113 and *C2cd3* are implicated in recruiting certain IFT-B subunits to the basal body, but the specificity
114 of these proteins for IFT recruitment is hard to discern, as only a small subset of IFT proteins has
115 been examined in these mutants and these proteins have pleiotropic roles in ciliogenesis³⁰⁻³².

116
117

118 Here, we combine proteomics, *in vivo* cell biology, mouse models and human genetics to
119 characterize a novel mechanism governing basal body recruitment and assembly of IFT-A. This
120 novel regulatory module is formed by specific protein-protein interactions among *Intu*, *Fuz*, and
121 *Wdpcp*, well-conserved proteins that control planar cell polarity (PCP) in *Drosophila* and govern
122 ciliogenesis in vertebrates³³⁻³⁷ (Fig. 1A). We term this new module the “CPLANE,” for ciliogenesis
123 and planar polarity effectors. We show that this module also includes the poorly understood

124 ciliopathy protein Jbts17, which we show recruits CPLANE to basal bodies where it acts
125 specifically by recruiting the IFT-A peripheral proteins. In the absence of CPLANE function, the
126 IFT-A core denuded of peripheral components still undergoes normal bi-directional transport,
127 though the movement of IFT-B is severely impaired. Finally, examination of mutant mice and
128 ciliopathy alleles from human patients reinforce the connection between CPLANE proteins, Jbts17,
129 and the IFT-A machinery, demonstrating that CPLANE plays a broad and essential role in
130 ciliogenesis and human ciliopathies.

131
132
133
134
135
136
137
138
139

Results:

140 Intu, Fuz, and Wdpcp are deeply conserved and are essential for vertebrate ciliogenesis (Fig.
141 1a)^{36,37}. To gain unbiased insights into their molecular functions, LAP-tagged versions of each
142 were stably expressed in ciliated mouse kidney IMCD3 cells, lysates were prepared, and
143 interacting proteins were affinity purified (Supplementary Fig. 1a,b). In addition, similar
144 experiments were performed using diverse IFT-A and ciliopathy related proteins as baits. Mass-
145 spectroscopy revealed the enrichment of the bait protein for each pull-down (Supplementary
146 Fig.1c, d; Supp. Dataset 1), and none of the baits were copurified with over 30 unrelated
147 control proteins, although all baits did bring down common contaminants (Supplementary
148 Fig. 1e). From this experiment, we identified a set of roughly 250 proteins that were
149 individually pulled down by each of the three CPLANE proteins (Supplementary Fig. 2a).

151
152

The CPLANE interactome.

153
154
155
156

157 We identified an extensive interaction network for the CPLANE proteins that involved a wide
158 array of protein machines, including dynein subunits, clathrin adaptors, and chaperonins, among
159 others (Fig. 1b and Supplementary Fig. 2b-d). Given that CPLANE proteins are essential for
160 vertebrate ciliogenesis^{36,37}, we were surprised to find only selective links to known ciliogenesis
161 proteins. No links were found within the combined CPLANE interactome to many major ciliary
162 machines, including the IFT-B complex, the BBSome, the inversin compartment, and transition

163
164
165 zone B9 complex. An exception was the intraflagellar transport complex A (IFT-A), as between
166 them, pulldown for Intu, Fuz and Wdpcp identified all six subunits of the IFT-A complex (Fig. 1b,
167 c and Supplementary Fig. 2c), though no IFT-B proteins were found. Moreover, while pulldown
168 of IFT-A proteins themselves also efficiently returned other IFT-A proteins, pulldowns with six
169 other ciliogenesis-related baits did not (Supp. Fig. 1d). These data suggest that CPLANE may
170 regulate IFT-A function, which we address below.

171
172
173 Most strongly enriched in all CPLANE pulldowns were the CPLANE proteins themselves, with
174 Intu, Fuz, and Wdpcp reciprocally co-purified in all combinations (Supp Figs. 1c and 2d; Supp.
175 Table 1). By contrast, these three proteins were entirely absent from pull-downs of six additional
176 ciliopathy related proteins (Supp. Fig. 1c). Interaction among some CPLANE proteins has also
177 been observed in high-throughput screens of human proteins^{38,39}. Moreover, the interactions
178 are conserved in *Drosophila*⁴⁰, though these proteins have no apparent role in ciliogenesis in
179 that animal. In addition, the Rsg1 GTPase, which we had previously observed as a Fuz
180 interacting protein^{38,39,41}, was also strongly associated with Intu and Wdpcp (Supp. Fig. 1c).

182
183
184 Finally, among the most strongly enriched proteins in the CPLANE interactomes was the largely
185 uncharacterized ciliopathy protein Jbts17 (also called C5orf42)(Fig. 1b and Supplementary Figs.
186 1c and 2c). This novel protein is associated with Joubert, Oral-Facial-Digital (OFD), and Meckel
187 Gruber syndromes⁴²⁻⁴⁵, and one recent paper identifies it as a component of the transition
188 zone⁴⁶. We confirmed interaction between Jbts17 and all three CPLANE proteins by co-IP of *in*
189 *vitro* translated proteins (Supp. Fig. 2e). Because so little is known of Jbts17, we explored its
190 link to the CPLANE proteins in more detail.

191
192
193

194 **CPLANE protein localization at the base of cilia.**

195
196
197
198 Jbts17 is evolutionarily conserved (Fig. 1a) and implicated in varying ciliopathies, but its function
199 remains largely undefined. In *Xenopus*, *Jbts17* was expressed in ciliated tissues (not shown),
200 and knockdown using anti-sense morpholino-oligonucleotides (MOs) to disrupt splicing resulted
201 in ciliopathy-related developmental defects, including failure of neural tube closure, defective
202 Hedgehog signaling, and defective left/right patterning (Fig. 2a-c and Supplementary Fig. 3a,b).
203 Accordingly, ciliogenesis was disrupted in the developing neural tube, in the node, and in
204 multiciliated cells (MCCs)(Fig. 2d-f). CRISPR-based disruption of *Jbts17* also disrupted
205 ciliogenesis, and co-injection of mRNA encoding GFP-Jbts17 rescued both the neural tube

206
207
208
209
210
211
212
213
214
215
216
217
218
219
220
221
222
223
224
225
226
227
228
229
230
231
232
233
234
235
236
237
238
239
240

defects and ciliogenesis defects resulting from MO-based knockdown (Fig. 2f and Supplementary Fig. 3a, h).

Given the physical association of Fuz, Intu, and Wdpcp with Jbts17 and Rsg1 (Supp. Fig. 1c), we explored the interrelationships among these proteins in *Xenopus* MCCs, which provide an effective platform for *in vivo* ciliary cell biology. Intu, Fuz, Rsg1, and Jbts17 localized robustly around basal bodies but were difficult to detect in axonemes (Fig. 2g). Super-resolution imaging revealed that GFP-Jbts17 was present in a ring surrounding the basal body, as marked by centrin4-BFP; this ring was similar to that formed by the distal appendage marker Cep164 (Fig. 2h). However, Jbts17 knockdown did not significantly affect recruitment of the distal appendage proteins Cep164 or Ofd1, the transition zone marker Mks1, or the basal body docking protein Hook2 (Supplementary Fig. 3g).

To assess the functional relationships of these proteins, we knocked each CPLANE protein down using MOs previously validated by mouse knockouts (see Methods) and then examined basal body localization of the remaining CPLANE members. Our data place Rsg1 at the bottom of the hierarchy: Its localization was lost from basal bodies after knockdown of any CPLANE protein, yet its own knockdown did not affect basal body recruitment of any other component (Fig. 2j and Supplementary Fig. 3c-f). Wdpcp and Intu held clear positions upstream of Fuz and Rsg1, but downstream of Jbts17. Interestingly, Wdpcp and Intu were also each required for the other's basal body localization. The role of Fuz was more complicated; unlike the other CPLANE proteins Fuz did not require Jbts17 for localization to basal bodies, and while loss of Fuz did disrupt basal body localization of Intu and Rsg1, it did not affect Wdpcp. These data provide an initial framework for the hierarchy of CPLANE protein functions.

A Jbts17 disease allele disrupts Intu localization.

Jbts17 is mutated in ciliopathies, so we asked if a disease-causing allele of Jbts17 would disrupt CPLANE function by examining a *Xenopus* cognate of a human Joubert syndrome-associated truncation of Jbts17. The R1569* truncation (equivalent to R1602 in humans⁴⁵; Supp. Fig. 4a) failed to localize to basal bodies, though another disease associated truncation R2406* localized normally, allowing us to map the basal body localization domain of Jbts17 to amino acids 1770-2318 (Supp. Fig. 4b). The pathogenicity of the R1569* truncation was apparent, because while expression of full-length Jbts17 efficiently rescues NTDs resulting from Jbts17

248
249
250 knockdown, expression of Jbts17-R1569* did not (Supplementary Fig. 3a). Linking this
251 embryological defect to cell biological function, Jbts17-R1569* also failed to localize to basal
252 bodies (Supplementary Fig. 4b) and unlike wild type, expression of Jbts17-R1569* could not
253 rescue basal body recruitment of Intu after Jbts17 knockdown (Supplementary Fig. 4c). Thus,
254 the Jbts17 disease allele fails to support CPLANE localization and function.

255
256
257
258
259
260

CPLANE recruits peripheral IFT-A proteins to basal bodies.

261 To understand the mechanisms by which CPLANE proteins impact ciliogenesis, we returned to
262 our proteomic dataset. We were intrigued by associations between CPLANE proteins and the
263 IFT machinery (Fig. 1b), because while we previously implicated Fuz and Rsg1 in IFT^{47,48}, their
264 mechanism of action remained ill-defined. CPLANE proteins did not interact with IFT-B
265 components, but rather specifically interacted with both the IFT-A core and peripheral IFT-A
266 subunits (Fig. 1b and Supplementary Fig. 1c). Nothing is known about the regulation of
267 peripheral sub-unit interaction with the IFT-A core, but we reasoned that by interacting with
268 both, CPLANE could facilitate IFT-A function. Because CPLANE localizes to basal bodies, we
269 tested this notion by assessing basal body recruitment of all six IFT-A proteins after CPLANE
270 disruption.

271
272

273 Strikingly, Jbts17 knockdown specifically disrupted the recruitment of the peripheral IFT-A
274 subunits to the basal body. The levels of lft139, lft121 and lft43 at basal bodies were
275 dramatically reduced after Jbts17 knockdown, though recruitment of the three IFT-A core
276 proteins lft140, lft144, lft122 was not disrupted (Fig. 3 and Supplementary Fig. 5a). In fact,
277 recruitment of lft122 was consistently increased (Fig. 3b,c). Though IFT-B is also composed of
278 core and peripheral components, Jbts17 knockdown did not disrupt recruitment of either the
279 peripheral IFT-B proteins lft20, lft80, and Cluap1, or the core IFT-B protein lft81 (Fig. 3c and
280 Supplementary Fig. 5b). Finally, the link between Jbts17 and IFT-A is likely relevant to disease
281 pathology, because while full-length Jbts17 expression rescued the loss of IFT-A basal body
282 recruitment after Jbts17 knockdown, the Joubert-associated Jbts17-R1569* truncation did not
283 (Supplementary Fig. 4d).

284
285
286
287
288
289
290
291
292
293
294
295
296
297

Defective IFT-B trafficking in the absence of CPLANE.

IFT particles exchange rapidly between axonemes and a cytoplasmic pool around the basal body, so we were curious to know what effect failure to recruit peripheral IFT-A proteins to basal bodies after CPLANE loss would have on IFT trafficking in the axoneme. We used high-speed confocal imaging to assess IFT in MCCs and found that disruption of either *Jbts17* or *Wdpcp* disrupted IFT-B movement, as we previously found for *Fuz*⁴⁷. Kymography revealed that both peripheral and core components of IFT-B formed stationary accumulations (Fig. 4a, b; Supplementary Fig. 5f), and quantitative microscopy confirmed a significant enrichment of total IFT-B levels in the axoneme (Supp. Fig. 5h).

298 These accumulations are reminiscent of the effect of genetic disruption of IFT-A^{9,10}. However,
299 the mechanisms by peripheral IFT-A proteins impact the movement of the IFT-A core has not
300 been examined in detail, and overall, very little is known about the dynamics of IFT-A in
301 vertebrates. We therefore also examined the effect of CPLANE loss on the dynamics of IFT-A
302 peripheral and core proteins in the axoneme. We found that peripheral IFT-A proteins that were
303 not recruited to basal bodies were likewise absent from axonemes after *Jbts17* knockdown,
304 consistent with a role for CPLANE in assembly of peripheral subunits onto the IFT-A core
305 (Supplementary Fig. 5e). By contrast, IFT-A core proteins were not only present in axonemes
306 at normal levels after *Jbts17* knockdown (Supp. Fig. 5d, 5h), but they also underwent bi-
307 directional transport (Fig. 4c, d; Supp. Fig. 5g), suggesting that the core was intact and could
308 associate with both anterograde and retrograde motors. Similar effects on IFT-A and IFT-B
309 were observed after *Wdpcp* knockdown (Supplementary Fig. 5f,g). These data suggest that
310 CPLANE acts by recruiting peripheral IFT-A proteins to the basal body for assembly onto the
311 IFT-A core.

312
313
314
315
316
317

OFD Syndrome phenotypes in mouse CPLANE mutants.

318 Together with our proteomic data from mammalian cultured cells, the *in vivo* imaging data from
319 *Xenopus* suggest that *Intu*, *Fuz*, and *Wdpcp* are intimately associated with *Jbts17*, which is the
320 major gene mutated in human Oral-Facial-Digital Syndrome Type 6 (OFD6)⁴³. Key diagnostic
321 features of OFD6 include high arched palate, tongue hamartoma, and polydactyly characterized

322
323
324 by Y-shaped metacarpals⁴⁹. Examining these same features in *Fuz* mutant mice, we
325 consistently observed high arched palates, lobulated tongues and Y-shaped metacarpals (Fig.
326 5a-d;f, h)(see also ref. ⁵⁰). We also observed Y-shaped metacarpals and defects in tongue and
327 palate morphology in *Wdpcp* mutants (Fig. 5e, g). These genetic data linking CPLANE
328 components to developmental defects characteristic of OFD are consistent with our proteomic
329 link between CPLANE and Jbts17.
330

331
332
333
334
335

Human CPLANE genes are mutated in diverse ciliopathies.

336 Our data argue for a functional and physical association of CPLANE proteins with Jbts17 on the
337 one hand, and with retrograde IFT machinery on the other. We therefore examined CPLANE
338 gene sequences in the exomes of human ciliopathy patients, focusing on OFD for its connection
339 to Jbts17 (Ref. ⁴³) and on Short-Rib Polydactyly Syndrome (SRPS) for its association to IFT-A
340 (Refs. ^{51,52}).
341
342

343 OFD VI, for which Jbts17 is the major gene⁴³, shares substantial phenotypic overlap with OFD
344 II, including high arched palate, tongue hamartomas, and Y-shaped metacarpals^{53,54}.
345 Consistent with our data above, exome sequencing of OFD patients with these characteristics
346 revealed disease-associated mutations in both *WDPCP* and *INTU*. In one patient, a 5-year-old
347 male presenting with facial dysmorphism, tongue hamartoma, high arched palate, tooth
348 abnormalities, and postaxial polydactyly, we found trans-heterozygous mutations in *WDPCP*.
349 One mutation was a frameshift (c.526_527delTT; Leu176Ilefs*21), and the other, a missense
350 mutation (c.160G>A; p.Asp54Asn) predicted to alter splicing by Human Splice Finder and ASSP
351 (Fig. 6a,b and Supplementary Table 2a). Sanger sequencing confirmed the variants and
352 compound heterozygosity for *WDPCP* by parental segregation (Fig. 6a). The altered aspartic
353 acid residue (D54) of *WDPCP* is highly conserved (Supplementary Fig. 6a) and has been
354 associated with atypical OFD in one previous patient⁵⁵, but no disease associated alleles of
355 *WDPCP* have yet been tested functionally. We therefore expressed these proteins in *Xenopus*
356 MCCs and found that the frame-shift allele resulted in total loss of protein, while the point
357 mutation led to a consistent but more modest defect in protein stability (Fig. 6c).
358

359
360

361 We also examined a 10-year-old male presenting with facial dysmorphisms, tongue nodular
362 tags, high arched palate, and bilateral central Y-shaped metacarpals (Supplementary Fig. 6b
363 and Supplementary Table 2a). Exome sequencing revealed a homozygous frameshift mutation

364
365
366 (c.396delT; p.Asn132Lysfs*11) in the *INTU* gene, and Sanger sequencing confirmed that the
367 homozygous *INTU* variant segregated with the phenotype (Supplementary Fig. 6c). Brain MRI
368 for both OFD patients showed no cerebellar abnormality, but cardiac ultrasound revealed aortic
369 coarctation and tetralogy of Fallot in OFD patients with *CPLANE* mutations (Supplementary
370 Table 2a), consistent with recent data implicating *CPLANE* genes in cardiac malformation⁵⁶.

371
372
373
374 In addition, we identified a homozygous missense mutation (p.Ala452Thr) in *INTU* in a child with
375 nephronophthisis and growth retardation. The boy, who presented with end-stage renal failure
376 at 10 yrs. of age, was the only affected child of three in a consanguineous family
377 (Supplementary Table 2a). The identified allele segregated with the affected status, and
378 homozygosity mapping revealed that the genomic locus of *INTU* was located within a stretch of
379 homozygosity on chromosome 4 (Supplementary Fig. 6d and data not shown). This change is in
380 a relatively poorly conserved residue (Supplementary Fig. 6e), suggesting that it may be a
381 hypomorphic allele. We also identified a heterozygous mutation (p.Glu365Gly) in *WDPCP* in a
382 boy with cerebellar vermis hypoplasia, ataxia, and retinal dystrophy (Supplementary Table 2a),
383 which may be a modifying allele contributing to this ciliopathy.

384
385
386 Finally, we examined exomes of individuals with SRPS and identified an affected patient with
387 compound heterozygosity for two *INTU* mutations confirmed by Sanger sequencing (c.
388 1063G>T; p.Glu355* and c. 1499A>C; p.Glu500Ala) (Fig. 6d, e; Supp. Fig. 6f). The affected
389 individual was born pre-term at 30-weeks with multiple congenital anomalies, including wide-
390 open fontanel, microphthalmia, tongue hamartomas, and tetralogy of Fallot (Supplementary
391 Table 2b). Radiographic analyses showed multiple skeletal anomalies, including short horizontal
392 ribs, shortened long bones with smooth edges, and pre-and post axial polydactyly (Fig. 6e and
393 Supplementary Table 2b). To confirm that the identified alleles caused the patient's disease, we
394 examined the function of the *INTU* mutants. The Glu355* allele failed to localize to basal bodies
395 when expressed in *Xenopus* MCCs (Fig. 6f), and while the Glu500A mutation did not affect
396 basal body localization, it did significantly impair the ability of the protein to recruit Ift43 (Fig 6g,
397 h).

398
399
400 Another case, presented with strikingly similar SRPS features (Supplementary Fig. 6g,h and
401 Supplementary Table 1b) and a single truncating mutation in *INTU* was confirmed by Sanger
402 sequencing (c. 826C>T; p.Gln276*). This change was inherited from the unaffected mother
403 (Figure S6i), but despite extensive analysis, no other changes were found in *INTU*. We

404
405
406 examined over 500 changes in the patient's genome that segregated with the phenotype, and
407 we found only a single change in a gene previously associated with SRPS, a heterozygous
408 change in *WDR35* (IFT121). This change (c.932G>T; p.Trp311Leu) was confirmed by Sanger
409 sequencing and was inherited from the unaffected father (Supplementary Fig. 6i), and this
410 residue is invariant in vertebrates (Supplementary Fig. 6j). The clinical presentation of this
411 patient was remarkably similar to the individual with compound heterozygosity for *INTU*
412 mutations (Supplementary Table 2b). The most striking similarity was the distinct polydactyly;
413 while most SRPS patients have 6-7 fingers and toes, these two patients both had 9-10. Thus,
414 while we cannot rule out a role for mutations in unknown ciliopathy genes, the known role for
415 *WDR35* in SRPS, our finding of a role for *INTU* in SRPS, and our finding of physical and
416 functional interactions between IFT-A and *CPLANE* lead us to suggest that SRPS in this patient
417 results from digenic inheritance of mutations in *WDR35* and *INTU*.

418
419
420
421
422
423
424
425
426
427
428
429
430
431
432
433
434
435
436
437
438
439
440
441
442
443
444
445
446
447
448
449
450
451
452
453
454
455
456
457
458
459

Discussion:

Here, we characterize an essential but poorly understood protein module, which we term CPLANE (Ciliogenesis and Planar Polarity Effector). The CPLANE proteins Intu, Fuz, and Wdpcp/Fritz are deeply conserved in animal evolution (Fig. 1a) and were first identified as PCP proteins in *Drosophila*^{33-37,40}. In vertebrates, mutation of these genes elicits ciliogenesis defects, and while their role in PCP remains murky, recent reports do suggest that Wdpcp and Intu may govern the localization of core PCP proteins⁵⁷⁻⁵⁹. Here, we combined proteomics in mammalian cell culture, *in vivo* cell biology in *Xenopus*, and genetic analysis in both mice and humans to demonstrate that the CPLANE is an important physical and functional unit governing a specific facet of ciliogenesis, namely the recruitment of IFT-A proteins to the base of cilia and the insertion of complete IFT-A particles into the axoneme (Fig. 7a,b).

Guided by our proteomic screen, imaging experiments here revealed that in the absence of CPLANE, peripheral IFT-A proteins fail to localize to basal bodies and do not assemble onto the IFT-A core. This connection between CPLANE and IFT-A is strengthened by genetic data linking CPLANE proteins to SRPS, which is generally associated with defects in IFT-A^{51,52}. CPLANE does not traffic along axonemes, arguing that it is not a component of the IFT particle itself, a result supported by the fact that CPLANE proteins associate relatively strongly with one another in our proteomic data, but comparatively weakly with IFT proteins (Supplementary Fig. 1c). Together, these data argue that CPLANE facilitates IFT-A recruitment and assembly at basal bodies, though the precise mechanisms by which it acts remain to be determined.

One possibility is that CPLANE may direct cytoplasmic transport of IFT-A proteins to the base of cilia. This idea is supported by the many links to cytoplasmic dynein machinery in our proteomics (Fig. 1; Supp. Fig. 2). A second line of evidence comes from computational modeling of protein structures (see Methods), which suggests that CPLANE proteins contain structural domains common in vesicle trafficking machinery (Supp. Fig. 7). Fuz contains a longin domain, and Intu is predicted to fold into a Sec23/24 domain. Likewise, Wdpcp is predicted to form an alpha solenoid attached to a beta-propeller, a configuration present in coat proteins, as well as IFT and BBSome subunits⁶⁰. Finally, Jbts17 is an enormous protein (3167 amino acids) and can be threaded onto multiple protein models, including a Sec23/24 fold, a beta propeller fold, and an importin domain.

On the other hand, the CPLANE proteins may instead impact IFT-A at the level of protein stability and assembly. This possibility is supported by our proteomic data linking Intu, Fuz, and Wdpcp individually to all eight subunits of the CCT chaperone complex (Fig. 1b; Table 1). This latter

460 mechanism would be particularly intriguing, because similar mechanisms have been proposed
461 linking protein folding to assembly of dynein arms^{22,23} and the BBSome^{27,28}. Importantly, as is
462 true for the CPLANE proteins, disruption of cytosolic assembly factors for dynein arms and the
463 BBSome also cause ciliopathies. This latter possibility is especially exciting because, despite this
464 long history of study, cytosolic factors facilitating basal body recruitment and assembly of IFT
465 particles have not been described.

466
467
468 We also found that peripheral IFT-A proteins were not present in axonemes after CPLANE
469 knockdown, though IFT-A core proteins entered axonemes and trafficked bi-directionally.
470 Because we also observed accumulations of IFT-B in axonemes similar to that following direct
471 disruption of IFT-A⁹⁻¹¹, our data argue that the peripheral components are essential for
472 association of IFT-B with IFT-A, at least during retrograde transport (Figs. 7a,b). This role for the
473 peripheral IFT-A proteins raises interesting questions concerning the mechanism of IFT-B
474 anterograde transport, because biochemical data suggest that heterotrimeric kinesin also
475 associates with IFT particles via the IFT-A^{7,13}. Given that IFT-B moves into axonemes and
476 accumulates there after CPLANE knockdown (Supp. Fig. 5c), it may be that the role for
477 peripheral proteins in linking IFT-A to IFT-B is specific to retrograde transport, consistent with
478 the known remodeling of IFT particles upon turnaround^{11,12}. Alternatively, homodimeric kinesin 2
479 associates directly with IFT-B in *C. elegans*, and while the situation in vertebrates is less
480 clear^{61,62}, IFT-B could move into cilia after CPLANE knockdown via direct association with the
481 homodimeric Kif17. Finally, the role for diffusion in axonemal transport is only now coming into
482 focus^{20,63}, so it is at least possible that IFT-B in these cases moves in the axoneme could move in
483 such a manner.

484
485 Finally, our data implicate CPLANE in diverse ciliopathies. Because SRPS is generally
486 associated with disruption of IFT-A^{51,52}, our identification of *INTU* mutations in SRPS patients
487 provides a genetic complement to our proteomic and cell biological linkage of CPLANE to IFT-A.
488 Our identification of CPLANE mutations in OFD patients similarly parallels the physical and
489 functional association of CPLANE with Jbts17. Additional insights into the mechanism of
490 CPLANE mutation in human disease will certainly emerge as we venture deeper into the
491 CPLANE protein interaction network. For example, *Wdpcp* mutations have been found in at
492 least one patient with Bardet-Biedl Syndrome³⁶, so the links between CPLANE proteins and
493 CCT are interesting since BBS6, 10 and 12 also interact with CCT^{27,28}. Our data may also shed
494 light on the still murky role of *FUZ* in human neural tube defects⁶⁴. Finally, our data suggest that
495 the CPLANE may be relevant not only to congenital defects, but also to infectious disease, since
496 recent data link *Fuz* and the endocytic machinery to alphavirus entry⁶⁵, and we observed
497 extensive interactions between

498 CPLANE and the vesicle trafficking machinery (Fig. 1b; Supp. Fig. 2b). In sum, our data
499 establish the CPLANE as a novel ciliogenic protein module with significant roles in
500 development and human disease.

501
502
503
504

Figure legends

505 **Figure 1. The CPLANE interactome.** (a) CPLANE proteins are deeply conserved in evolution;
506 numbers indicate percent identity (+additional percent similarity). “XX” indicates that reciprocal
507 BLAST identified no clear orthologue. (b) The extended CPLANE protein network. Tandem
508 affinity purification of Intu, Fuz, Wdpcp, IFT-A¹⁵, and the published NPHP network⁴ were
509 assembled, thresholded for most likely network members, and over 2200 nodes arranged in
510 Cytoscape, with 78 nodes presented here. The raw peptide data for this network will be
511 deposited in the appropriate databases upon acceptance of the manuscript.

512

513 **Figure 2. Jbts17 localizes to the base of cilia and is required for ciliogenesis and cilia-**
514 **mediated patterning.** (a) RT-PCR demonstrates disrupted Jbts17 splicing after MO injection.
515 ODC1 = loading control. (b) *In situ* hybridization of SHH direct target, *nkx2.2* in Jbts17-knockdown
516 (st. 22). (c) *Pitx2* expression at st. 26. Arrows indicate signal in left lateral plate mesoderm
517 (LPM); graph indicates *pitx2* expressing embryos. (d) Acetylated α -tubulin immunostaining in the
518 ventral neural tube (st. 22)(Scale bars, 10 μ m). (e) Nodal cilia length is reduced; cilia numbers are
519 unchanged. (Scale bars, 10 μ m). Graphs in D and E each show pooled data from two
520 independent experiments cilia length (mean +/- SEM; ***p <0.001). (f) Multi-ciliated cells in
521 control, Jbts17-knockdown (Jbts17-KD), and rescue with untargeted Jbts17 mRNA. Cilia and
522 cell membrane visualized by GFP-CFAP20 (green) and membrane-RFP (magenta). Scale
523 bars, 10 μ m. (g) GFP-tagged Jbts17 localizes near basal bodies (visualized by co-expressed
524 centrin4-RFP) in an MCC (scale bar, 10 μ m). (h) Super-resolution image of GFP-Jbts17 and
525 mCherry-Cep164 at a single basal body; both form rings of ~260nm around the basal body,
526 visualized by centrin4-BFP. Diameters shown as mean \pm SD in each panel. The lower graph
527 shows fluorescence intensities for GFP-Jbts17, mCherry-Cep164, and centrin4-BFP (Scale bar,
528 100 nm). (i) GFP-tagged CPLANE proteins (green) and basal bodies visualized by centrin4-RFP
529 (magenta) in control and Jbts17 knockdown multi-ciliated cells; box plots of CPLANE intensities
530 at basal bodies; boxes extend from 25th-75th percentiles, with a line at the median; whiskers indicate
531 max and min. (j) Table summarizes the localization of CPLANE proteins at basal bodies for
532 each knockdown (see Supplementary Fig. 2c-f).

533

534 **Figure 3. Jbts17 is necessary for recruitment of peripheral IFT-A proteins to basal bodies.**
535 (a) *Ift43* localization at basal bodies in *Xenopus* MCCs as marked by centrin4-RFP is lost in
536 MCCs after Jbts17 knockdown. (b) Peripheral IFT-A components are not recruited to centrin4-
537 RFP labeled basal bodies after Jbts17 knockdown. (c) Quantification of IFT protein localization
538 to basal bodies from two independent experiments. Graphs show fluorescence intensity of GFP
539 fusions to indicated IFT proteins normalized against that of centrin4-RFP (see methods).
540 Peripheral IFT-A proteins are specifically lost after Jbts17 knockdown.

541

542 **Figure 4. Jbts17 is required for bi-directional axonemal transport of IFT-B particles, but**
543 **not the core IFT-A.** Still images from high-speed time-lapse movies of IFT using GFP fusion to
544 IFT proteins (green) and membrane-RFP (magenta). Cluap1-GFP in control embryo (a) and
545 Jbts17 morphant (b). GFP-IFT144 in control (c) and Jbts17 morphant (d). Insets show high
546 magnification views of localization of IFT particles in a single axoneme in the boxed regions.

547
548
549

550 Scale bars = 10 μ m. Associated kymograph representing movements of IFT particles are shown
551 in panels a'-d'.

552

553 **Figure 5. CPLANE mutant mice display diagnostic features of Oral-Facial-Digital**
554 **Syndrome Type 6.** (a and b) Frontal sections at E14.5 reveal that *Fuz* mutant mice display high
555 arched palate (arrow) and lobulation of the tongue (arrowheads). (c and d) *Fuz* mutant mice
556 display develop polydactyly with Y-shaped metacarpals. (e) *Wdpcp* mutant mice display develop
557 polydactyly with Y-shaped metacarpals. (f, g, h) Frontal sections of E13.5 Wildtype, *Wdpcp* and
558 *Fuz* mutant embryos. DAPI labels nuclei (cyan). (f', g', h') Illustrations highlighting the
559 corresponding palatal condensations (purple) and tongue (pink) in F-H. Mutant palatal
560 condensations form more medially than do controls and fail to extend into the mouth (See
561 Tabler et al., 2013).

562

563 **Figure 6. CPLANE mutations in human ciliopathies.** (a) Pedigree showing *WDPCP*
564 mutations in an OFD patient. (b) The patient displays tongue hamartomas and dental anomalies.
565 (c) When expressed in *Xenopus* embryos, the D54A allele of human *WDPCP* produces less
566 protein compared to wild-type; the L176F-fs26* allele produces no protein. (d) Pedigree showing
567 *INTU* mutations in an SRPS phenotype. (e) X-ray of the patient. (f) The E355* allele of *INTU*
568 disrupts basal body localization. (g and h) Wild-type *Intu* rescues *Ift43* localization to basal
569 bodies after *Intu* knockdown; the E500A allele of *Intu* does not. Data shown are pooled from three
570 independent experiments.

571

572 **Figure 7. Models for CPLANE function and structure.** (a) Schematic of normal IFT.
573 Peripheral proteins are assembled onto the IFT-A core in the cytoplasm and injected together
574 with IFT-B for bi-direction transport in axonemes. (b) In the absence of CPLANE, IFT-A core
575 particles lacking peripheral proteins are injected into axonemes and traffic normally; IFT-B
576 enters axonemes but fails to move in a retrograde direction and accumulates.

577

578

579

580

581

582

583

Experimental procedures:

584 Details of the experimental procedures can be found in the Supplementary Material online.
585 Briefly, the methods used here were essentially those described previously.
586 Immunoprecipitation of LAP-Tagged CPLANE proteins was performed as described in ref. ⁴.
587 General methods for experiments with *Xenopus* were performed as described in ref ^{36,37}.
588 Specifically, imaging of IFT proteins at basal bodies and time-lapse imaging of IFT were
589 performed as per Ref. ⁴⁷. Exome sequencing was performed essentially as per Ref. ⁴ and Ref.
590 ⁴³.

591

592

593

Online Supplementary Experimental Procedures:

594

595

Tandem Affinity Purification and Mass Spectrometry

596 To best optimize the LAP purification procedure and minimize the possibility of carryover, we have
597 standardized the growth of cells, the preparation of extracts, and the method of tandem affinity
598 purification (Torres et al., 2009). Briefly, stable LAP cell lines were harvested using detergent. The
599 mIMCD-3 (ATCC® CRL-2123™) cell line was obtained from ATCC. The renal IMCD3 line was
600 authenticated by expression of renal markers (AQP2), polarization, establishment of tight
601 junctions, and ciliation, as outlined in (REF). Lysates were clarified at 43,000 rpm and subjected to

602 anti-GFP immunoprecipitation. Bound proteins were eluted from antibody beads using TEV
 603 protease, recaptured on S-protein agarose (Novagen), and eluted in 4x NuPAGE sample buffer
 604 (Invitrogen). Following purification, great care is taken to ensure a lack of contamination from both
 605 environmental sources and from other purified proteins. Each purified set of interacting proteins is
 606 separated on an individual 10% Bis-Tris polyacrylamide gel and stained with Coomassie brilliant
 607 blue. IMCD3 samples were run into gels for 20-40mm and divided into 20-40 x1 mm slices. Each
 608 excised lane was reduced, carboxyamidomethylated and digested with trypsin. Peptide
 609 identification of each digestion mixture was performed by microcapillary reversed-phase HPLC
 610 nanoelectrospray tandem mass spectrometry (mLC-MS/MS) on an LTQ-Orbitrap Velos or XL
 611 mass spectrometer (ThermoFisher Scientific, San Jose, MA). The Orbitrap repetitively surveyed an
 612 m/z range from 395 to 1600, while data-dependent MS/MS spectra on the twenty (Velos) or ten
 613 (XL) most abundant ions in each survey scan were acquired in the linear ion trap. MS/MS spectra
 614 were acquired with relative collision energy of 30%, 2.5-Da isolation width, and recurring ions
 615 dynamically excluded for 60 s. Preliminary sequencing of peptides was facilitated with the
 616 SEQUEST algorithm with a 30 ppm mass tolerance against a species specific (mouse or human)
 617 subset of the UniProt Knowledgebase. With a custom version of the Harvard Proteomics Browser
 618 Suite (ThermoFisher Scientific, San Jose CA), peptide spectrum matches (PSMs) were accepted
 619 with mass error < 2.5ppm and score thresholds to attain an estimated false discovery rate (FDR) of
 620 <1% using a reverse decoy database strategy. For IMCD3-LAP-GFP control samples, peptide
 621 identification was performed using NanoAcquity UPLC (Waters Corp, Milford, MA). Samples were
 622 analyzed on-line via nanospray ionization into a hybrid LTQ-Orbitrap mass spectrometer (Thermo
 623 Scientific, San Jose, CA). Data were collected in data dependent mode with the parent ion being
 624 analyzed in the FTMS and the top 8 most abundant ions being selected for fragmentation and
 625 analysis in the LTQ. Tandem mass spectrometric data were analyzed using the Mascot search
 626 algorithm (Matrix Sciences, London, UK) against the mouse Uniprot database (including reverse
 627 hits and contaminants) and filtered to a 5% FDR.

628

629 TAP/MS data network generation

630 For individual genes identified in each AP/MS sample, we calculated the normalized spectral
 631 abundance factor (NSAF)

$$NSAF = \frac{P_g/L_g}{\sum_i P_i/L_i}$$

632

633 Where P_g represents the number of spectral counts mapped to gene g , and L_g is the mean length,
 634 in residues, of reference protein isoforms derived from that gene. The P/L quotient is normalized to
 635 the sum of P/L quotients for all genes in the dataset, excluding those derived from the bait protein
 636 and those derived from known exogenous proteins. We exclude, for example, proteins commonly
 637 found in skin and enzymes added during sample preparation. Using an unpublished set of eight
 638 negative control datasets, we systematically search for genes whose score in an experimental
 639 data set is highly unlikely. These filtered genes included in the attached Cytoscape
 640 (<http://www.cytoscape.org>) network file, and a manually curated, simplified subset of these are
 641 shown in Figure 1b.

642

643 *Xenopus* embryo manipulations and microinjections

644 Female adult *Xenopus laevis* were induced to ovulation by injection of human chorionic
 645 gonadotropin, and eggs were fertilized *in vitro*, dejellied in 3% cysteine (pH 7.9) at 2-cell stage,

646 and subsequently reared in 0.3× Marc's Modified Ringer's (MMR) solution. For microinjections,
647 embryos were placed in a solution of 2% Ficoll in 0.3× MMR and handled using forceps and an
648 Oxford universal micromanipulator. After injections, embryos were reared for 3 hr in 2% Ficoll in
649 0.3× MMR and then washed and reared in 0.3× MMR until the appropriate stages. All experiments
650 were repeated in multiple embryos from multiple clutches, as is standard in the field. No explicit
651 randomization or blinding strategy was employed. Sex cannot be practically determined for
652 tadpoles used in these studies. This work was carried out with approval of the University of Texas
653 Animal Care and Use Committee.

654

655 **Morpholinos, mRNA, and gRNA injections**

656 Capped mRNA was synthesized using mMACHINE kit (Ambion). mRNA and
657 antisense morpholino were injected into two ventral blastomeres or two dorsal blastomeres at the
658 4-cell stage to target the epidermis or the neural tissues, respectively⁶⁶. Morpholino sequences
659 and the working concentrations include:

660 We note that the *Intu*, *Fuz*, and *Wdpcp* MO used here elicit phenotypes validated by genetic
661 disruption of these genes in mice^{36,37,57,67}. The *Rsg1* MO has been validated by disruption of the
662 *Rsg1* GTPase by expression of a dominant-negative mutant⁴¹.

663

664 **Plasmid Constructs**

665 Three cDNA fragments encoding *Xenopus laevis* *Jbts17* were amplified by PCR from stage 25
666 *Xenopus* cDNA library with the primers

667 These three PCR products were then fused to generate full-length cDNA by PCR with *Sma*I and
668 *Not*I restriction enzyme sites at 5 and 3 prime ends, respectively. Truncated mutants were
669 generated by PCR. The cDNAs were then subcloned into various pCS107 vectors that established
670 fusion with either EGFP, mRFP, or myc-tag at the N-terminus.

671 Full-length *Ofd1*, *Cep164*, *Hook2*, *Mks1*, *IFT122*, *IFT140*, *IFT144*, *IFT43*, *IFT121*, *IFT139*, *IFT81*,
672 *IFT80* and *Cluap1* cDNAs were identified in Xenbase⁶⁸ and amplified by PCR and sub cloned into
673 pCS107 vectors fused with GFP, RFP, or mCherry at their N-termini. *Rsg1*, *IFT20*, *IFT43*,
674 *Centrin4* and *Inturned* constructs were previously described in^{47,48,69}. GFP-tagged CFAP20 was
675 kindly gifted from Dr. Brian Mitchell (Northwestern Univ.).

676

677 **In vitro protein translation and pull down assay**

678 GFP-tagged *Inturned*, *Fuzzy*, *WDPCP* and Flag-tagged *Jbts17* (907-1569) proteins were
679 synthesized using a TnT® SP6 Coupled Wheat Germ Extract System (Promega). After
680 centrifugation at 17,000 *g* at 4°C for 10 minutes, the synthesized soluble proteins were mixed and
681 incubated in binding buffer (20 mM Tris-HCl pH 8.0, 1 mM EDTA, 1 mM DTT and 150 mM NaCl)
682 for 2 hr at 4°C. Flag-tagged *Jbts17* protein was precipitated by anti-Flag M2 magnetic beads
683 (Sigma-Aldrich). The beads were washed with binding buffer containing 0.1% Triton X-100 four
684 times and eluted with 200 ng/ml of Flag peptide in 1x TBS. The eluted proteins were analyzed by
685 immunoblotting with anti-GFP (Abcam) and anti-Flag M2 (Sigma-Aldrich) antibodies.

686

687 **sgRNA synthesis, Cas9 induced genomic editing and genotyping**

688 Cas9-CRISPR mediated genome editing in *Xenopus* was previously described (Nakayama et al.,
689 Methods Enzymol 546:355-75 (2014)).

690 oligonucleotides. The amplicon was purified by PCR purification kit (Qiagen) and used as a
691 template for sgRNA synthesis. sgRNA was generated by using T7 MEGAscript kit (Ambion) and
692 purified by MEGAclean Transcription Clean-up kit (Ambion). 1.25 ng of Cas9 protein (PNABIO) and
693 250 pg of sgRNA were injected into animal pole at 1-cell stage. Genomic DNA was extracted from
694 stage 25 embryos using DNeasy Blood & Tissue kit (Quiagen) following manufacturer's
695 protocol and the 468 bp of genomic region which contains the sgRNA target sequence was
696 amplified by PCR.

697 The genome editing efficiency by CRISPR was examined by T7 Endonuclease I (T7EI) assay and
698 NcoI digestion and analyzed by 2% agarose gel.

699

700 **Basal body imaging and quantification**

701 Fluorescence images of GFP, RFP or BFP fusion proteins at basal bodies in stage 25-28 multi-
702 ciliated cells were captured with LSM700 inverted confocal microscope (Carl Zeiss) with a Plan-
703 APOCHROMAT 63×/1.4 oil immersion objective.

704 The fluorescence intensities of GFP, RFP, or BFP fused proteins at basal bodies in slices from 2
705 mm of apical surface was measured by the 3D object counter plug-in of Fiji software as described
706 previously^{47,48}. The Object size was set to 20, and threshold was determined empirically to
707 maximize detection of apparent foci. At least 14 basal bodies/cells from at least 12 cells in 4
708 independent embryos were analyzed. Statistical analysis was subsequently performed, making
709 use of the Student t-test.

710

711 **Live imaging of IFT particles and analysis**

712 For high-speed *in vivo* imaging, *Xenopus* embryos injected with GFP-tagged IFT mRNAs and
713 membrane RNA were anaesthetized with 0.005 % benzocaine at stage 25-28. Images were
714 acquired on Nikon eclipse Ti confocal microscope with a 63×/1.4 oil immersion objective. Time-
715 lapse series were captured 266.5 msec per frame. Kymographs were generated and IFT velocities
716 measured in Fiji with the kymograph plugin.

717

718 **Super-resolution microscopy**

719 GFP-Jbts17, mCherry-Cep164 and Centrin4-BFP were co-expressed by mRNA injection epidermis
720 in stage 27 *Xenopus* embryos. Fluorescence signals were captured by LSM 710/Elyra S.1 (Carl
721 Zeiss) via a 63×/1.3 oil-immersion objective. Raw fluorescence images were processed by
722 structured illumination algorithm using Zen software (Carl Zeiss). The arbitrary unit (a.u.) of
723 fluorescence intensities of ring-shaped structure of GFP-Jbts17 and mCherry-Cep164 at basal
724 bodies were measured by Plot Profile plugin in Fiji software.

725

726 **Immunostaining**

727 Immunostaining was performed as per ⁷⁰. Embryos were fixed in MEMFA for 2 hr at room
728 temperature after removing the vitelline envelop and washing with PBST (1 ×PBS containing
729 0.05% TritonX-100). Transverse sections of neural tube were generated using a Vibratome series
730 1000 from stage 22 embryos, and GRP region was manually dissected from stage 17 embryos
731 using forceps. Sections were dehydrated completely in methanol at -20 °C overnight. After
732 rehydration, sections were blocked with 10% fetal bovine serum in PBST for 60 min, incubated
733 with anti-acetylated- α -tubulin (1:2000, clone 6-11B-1, Sigma), and diluted in blocking solution.
734 Primary antibody was conjugated with an Alexa Fluor 488 goat anti-mouse IgG (Invitrogen).
735 Fluorescence images were obtained using Zeiss LSM700 confocal microscope. Cilia length in
736 neural tube and GRP was measured in Fiji software.

737

738 ***In situ* hybridization**

739 Whole mount *in situ* hybridization of *Xenopus* embryos was performed as described previously ⁷¹
740 using the Dig-labelled RNA probe against *nkx2.2*, *vax1* and *pitx2c*. Bright field images were
741 captured on a Zeiss Axiozoom V16 stereomicroscope.

742

743 **RT-PCR**

744 Jbts17 morpholino was injected into the all cells at 4-cell stage, and the total RNA was isolated
745 using TRIzol reagent (Invitrogen) from four stage 25 *Xenopus* embryos. The stage 25 cDNA
746 library was synthesized using M-MLV Reverse Transcriptase (Invitrogen) with random hexamers.
747 Jbts17 and an Ornithine decarboxylase 1 (ODC1) internal control were amplified using Phusion®
748 High-Fidelity DNA Polymerase (New England Biolabs) with following primers:

749 The abundance of the resulting amplicon was analyzed on a 2.0% agarose gel stained with
750 ethidium bromide under UV transilluminator.

751 **Protein structure modelling**

752 For fold recognition studies of Fuz, Intu, Wdpcp, Jbts17 and Rsg1, we used HHpred ⁷² and
753 pGenThreader ⁷³ with default parameters searched against the latest set of PDB structures. We
754 used the respective Modeller pipelines on the HHpred and pGenThreader servers to build
755 homology models based on high confident fold recognition results. Validity of the homology
756 models was checked using automated scores provided by HHpred. Additionally, DaliLite ⁷⁴ was
757 used to align the homology models with the original template for visual inspection of the fold.

758 **Human subjects**

759

760 The committees approving work with human subjects include the GAD collection n° DC2011-1332
761 (Thauvin-Robinet), Institutional Review Boards of the University of Michigan and Boston Children's
762 Hospital (Hildebrandt), and the Human Subjects Institutional Review Board of the University of
763 California at Los Angeles (Krakow). Informed consent was obtained from all study participants and
764 consent was obtained for use of all images of human subjects.

765

766

Acknowledgements:

767

768

769

770

771

772

773

774

775

776

777

778

779

780

781

782

783

784

785

786

787

788

789

Author Contributions:

790

791

792

793

794

795

796

797

798

799

800

801

802

803

804

805

806

807

808

809

We thank the patients and their families; the IntegraGen society for exome analysis; NHLBI GO Exome Sequencing Project which produced and provided exome variant calls for comparison: Lung GO Sequencing Project (HL-102923), WHI Sequencing Project (HL-102924), the Broad GO Sequencing Project (HL-102925), Seattle GO Sequencing Project (HL-102926) and Heart GO Sequencing Project (HL-103010). We thank Biological Resources Center – Ferdinand Cabanne (Dijon, France) for fibroblasts centralization and storage. Sequencing was provided by the University of Washington Center for Mendelian Genomics (UW CMG) and was funded by the NHGRI and NHLBI (Grant 1U54 HG006493) to Drs. Debbie Nickerson, Jay Shendure, and Michael Bamshad. This work was supported by grants from the following: Uehara Memorial Foundation Fellowship to M.T.; an NIDCR NRSA to J.M.T.; the French Rare Diseases Foundation, French Ministry of Health (PHRC national 2010-A01014-35 to C.T-R), and Regional Council of Burgundy to C.T.-R.; NIDDK (DK1068306) to F.H., who is an HHMI Investigator, a Doris Duke Distinguished Clinical Scientist, and the Warren E. Grupe Professor; NIAMS (AR061485) to J.C. ; BBSRC (BB/K010492/1) and MRC (MR/L017237/1) to K.J.L.; NIH, NSF, CPRIT, and the Welch Foundation (F-1515) to E.M.M.; R01AR066124, March of Dimes and Joseph Drown Foundation, NIH/NCATS UCLA CTSI Grant UL1TR000124 to D.K.; R01AR062651 to D.H.C.; NIGMS (GM114276), Baxter Laboratory, and Stanford Department of Research to P.K.J.; NIGMS and NHLBI to J.B.W., who was an HHMI Early Career Scientist.

Michinori Toriyama contributed to design, execution and interpretation of the overall research plan, with special emphasis on all frog embryo experiments and in vitro binding assays. He also contributed to writing the manuscript. Chanjae Lee designed, performed and interpreted live-imaging of IFT particles in axonemes and contributed to other imaging experiments in *Xenopus*. Kevin Drew and Edward M. Marcotte provided protein structural models. Jacqueline M. Tabler, Jiang Chen and Karen J. Liu contributed to design execution and interpretation of mouse genetic data. Marcus R. Kelley contributed to the execution and analysis of the proteomic data. Tae Joo Park contributed to *Xenopus* studies. S. Paige Taylor, Ivan Duran, Daniel H. Cohn, Ange-Line Bruel, Daniella Braun, Ghislaine Pierquin, Armand Biver, Kerstin Wagner, Anne Malfroot, Inusha Panigrahi, Brunella Franco, Hadeel Adel Al-lami, Yvonne Yeung, Yeon Ja Choi, University of Washington Center for Mendelian Genomics, Yannis Duffourd, Laurence Faivre, Jean-Baptiste Rivière contributed to collection of human patient and sequencing data. Friedhelm Hildebrandt, Christel Thauvin-Robinet, and Deborah Krakow contributed to design, execution and interpretation of human genetic data. Peter K. Jackson contributed to coordinating the overall research effort with a focus on design and interpretation of the proteomic screen and contributed to writing the manuscript. John Wallingford coordinated the overall research effort, oversaw experimental design and interpretation, and wrote the manuscript.

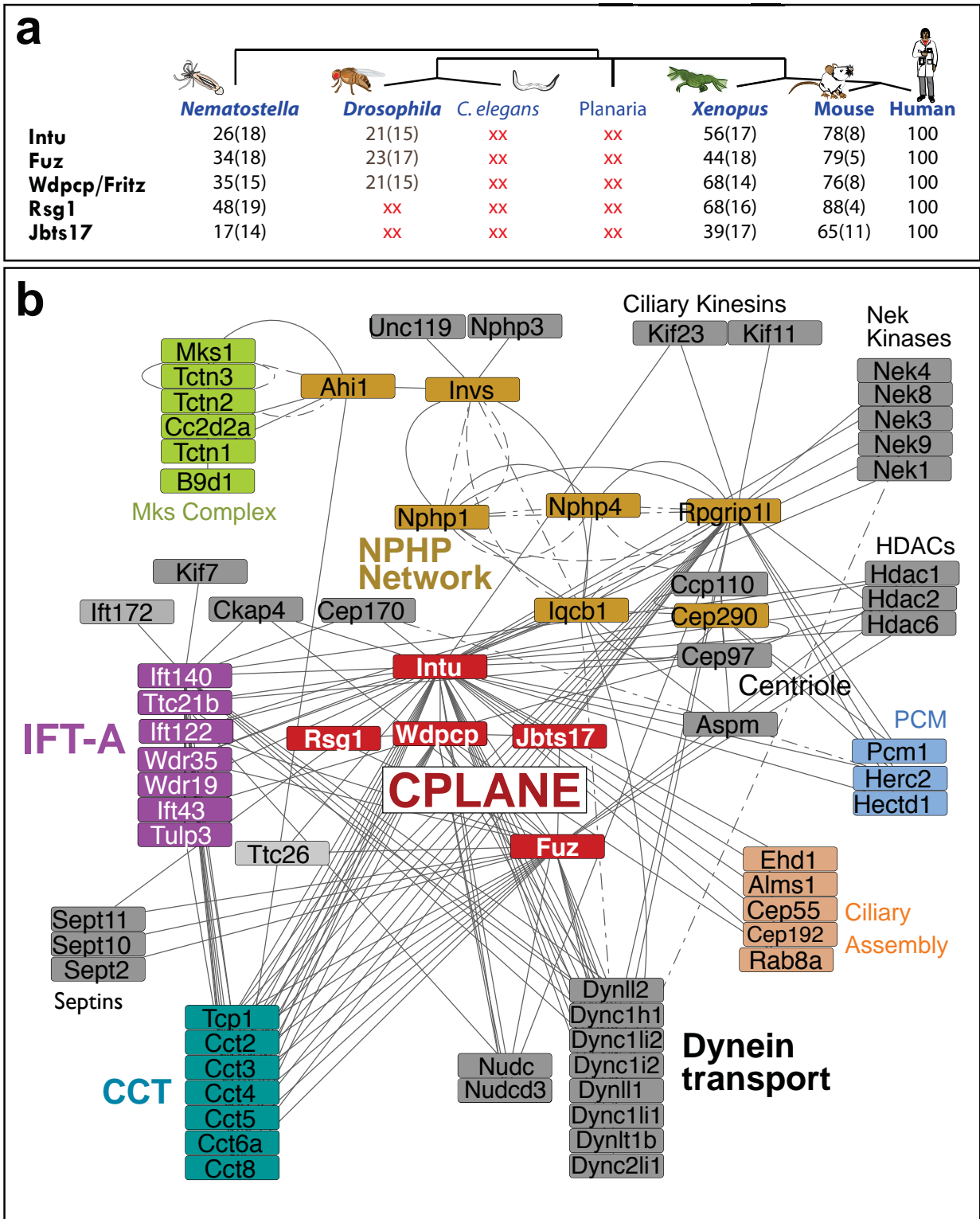
810
811812 **References:**813
814

- 815 1. Hildebrandt, F., Benzing, T. & Katsanis, N. Ciliopathies. *N Engl J Med* **364**, 1533-43 (2011).
- 816 2. Oh, E.C. & Katsanis, N. Cilia in vertebrate development and disease. *Development* **139**, 443-8
817 (2012).
- 818 3. Nachury, M.V. *et al.* A core complex of BBS proteins cooperates with the GTPase Rab8 to promote
819 ciliary membrane biogenesis. *Cell* **129**, 1201-13 (2007).
- 820 4. Sang, L. *et al.* Mapping the NPHP-JBTS-MKS protein network reveals ciliopathy disease genes and
821 pathways. *Cell* **145**, 513-28 (2011).
- 822 5. Garcia-Gonzalo, F.R. *et al.* A transition zone complex regulates mammalian ciliogenesis and ciliary
823 membrane composition. *Nat Genet* **43**, 776-84 (2011).
- 824 6. Kobayashi, D. & Takeda, H. Ciliary motility: the components and cytoplasmic preassembly
825 mechanisms of the axonemal dyneins. *Differentiation* **83**, S23-9 (2012).
- 826 7. Cole, D.G. *et al.* Chlamydomonas kinesin-II-dependent intraflagellar transport (IFT): IFT particles
827 contain proteins required for ciliary assembly in *Caenorhabditis elegans* sensory neurons. *J Cell*
828 *Biol* **141**, 993-1008 (1998).
- 829 8. Kozminski, K.G., Johnson, K.A., Forscher, P. & Rosenbaum, J.L. A motility in the eukaryotic
830 flagellum unrelated to flagellar beating. *Proc Natl Acad Sci U S A* **90**, 5519-23 (1993).
- 831 9. Pazour, G.J., Wilkerson, C.G. & Witman, G.B. A dynein light chain is essential for the retrograde
832 particle movement of intraflagellar transport (IFT). *J Cell Biol* **141**, 979-92 (1998).
- 833 10. Piperno, G. *et al.* Distinct mutants of retrograde intraflagellar transport (IFT) share similar
834 morphological and molecular defects. *J Cell Biol* **143**, 1591-601 (1998).
- 835 11. Iomini, C., Babaev-Khaimov, V., Sassaroli, M. & Piperno, G. Protein particles in *Chlamydomonas*
836 flagella undergo a transport cycle consisting of four phases. *J Cell Biol* **153**, 13-24 (2001).
- 837 12. Pedersen, L.B., Geimer, S. & Rosenbaum, J.L. Dissecting the molecular mechanisms of intraflagellar
838 transport in *chlamydomonas*. *Curr Biol* **16**, 450-9 (2006).
- 839 13. Rompolas, P., Pedersen, L.B., Patel-King, R.S. & King, S.M. *Chlamydomonas* FAP133 is a dynein
840 intermediate chain associated with the retrograde intraflagellar transport motor. *J Cell Sci* **120**,
841 3653-65 (2007).
- 842 14. Ou, G., Blacque, O.E., Snow, J.J., Leroux, M.R. & Scholey, J.M. Functional coordination of
843 intraflagellar transport motors. *Nature* **436**, 583-7 (2005).
- 844 15. Mukhopadhyay, S. *et al.* TULP3 bridges the IFT-A complex and membrane phosphoinositides to
845 promote trafficking of G protein-coupled receptors into primary cilia. *Genes Dev* **24**, 2180-93
846 (2010).
- 847 16. Liem, K.F., Jr. *et al.* The IFT-A complex regulates Shh signaling through cilia structure and
848 membrane protein trafficking. *J Cell Biol* **197**, 789-800 (2012).
- 849 17. Behal, R.H. *et al.* Subunit interactions and organization of the *Chlamydomonas reinhardtii*
850 intraflagellar transport complex A proteins. *J Biol Chem* **287**, 11689-703 (2012).
- 851 18. Lucker, B.F. *et al.* Characterization of the intraflagellar transport complex B core: direct interaction
852 of the IFT81 and IFT74/72 subunits. *J Biol Chem* **280**, 27688-96 (2005).
- 853 19. Taschner, M., Bhogaraju, S. & Lorentzen, E. Architecture and function of IFT complex proteins in
854 ciliogenesis. *Differentiation* **83**, S12-22 (2012).
- 855 20. Craft, J.M., Harris, J.A., Hyman, S., Kner, P. & Lehtreck, K.F. Tubulin transport by IFT is upregulated
856 during ciliary growth by a cilium-autonomous mechanism. *J Cell Biol* **208**, 223-37 (2015).
- 857 21. Bhogaraju, S. *et al.* Molecular basis of tubulin transport within the cilium by IFT74 and IFT81.
858 *Science* **341**, 1009-12 (2013).
- 859 22. Tarkar, A. *et al.* DYX1C1 is required for axonemal dynein assembly and ciliary motility. *Nat Genet*
860 **45**, 995-1003 (2013).
- 861 23. Omran, H. *et al.* Ktu/PF13 is required for cytoplasmic pre-assembly of axonemal dyneins. *Nature*
862 **456**, 611-6 (2008).
- 863 24. Mitchison, H.M. *et al.* Mutations in axonemal dynein assembly factor DNAAF3 cause primary ciliary

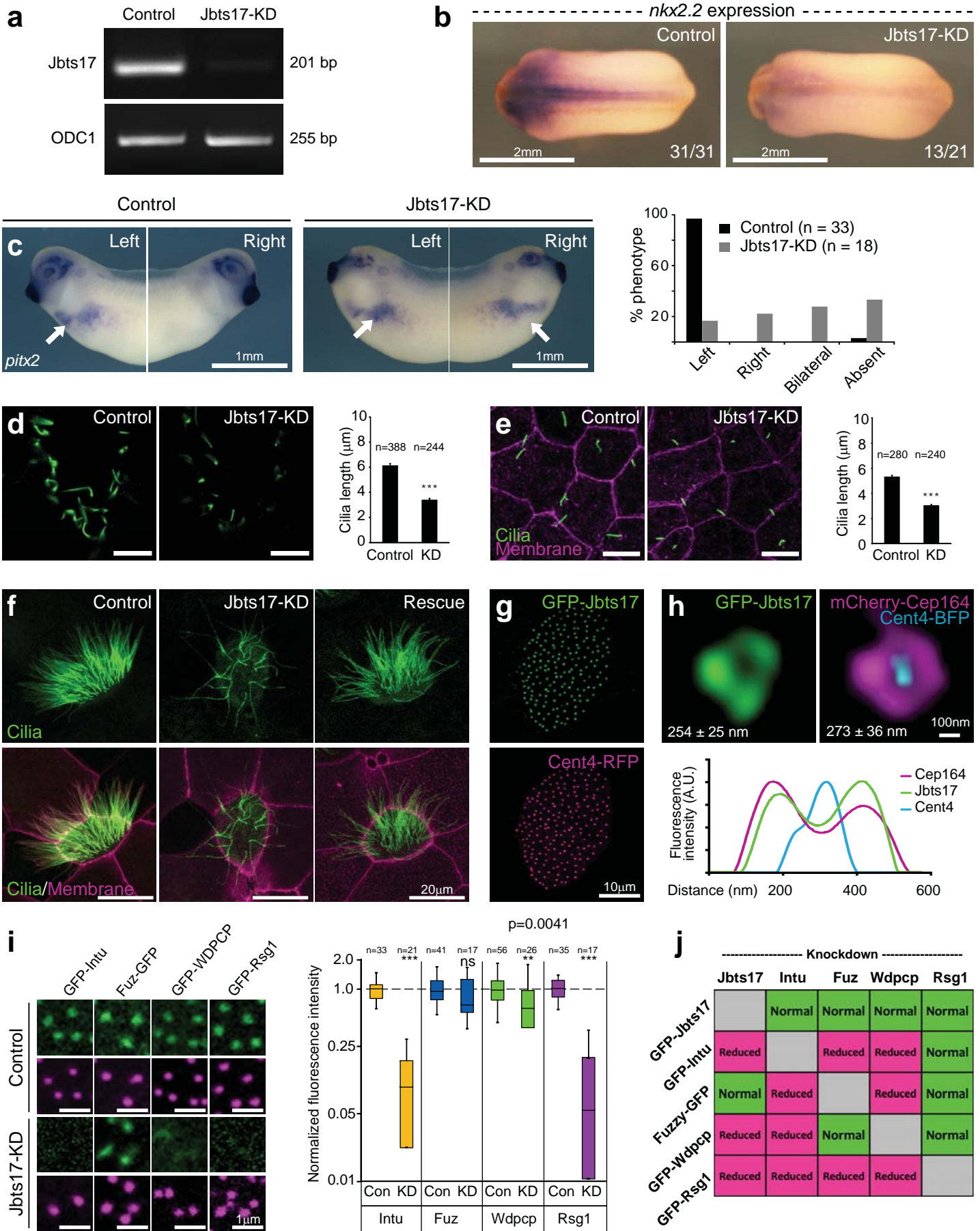
- 864 dyskinesia. *Nat Genet* **44**, 381-9, S1-2 (2012).
- 865 25. Horani, A. *et al.* Whole-exome capture and sequencing identifies HEATR2 mutation as a cause of
866 primary ciliary dyskinesia. *Am J Hum Genet* **91**, 685-93 (2012).
- 867 26. Diggle, C.P. *et al.* HEATR2 plays a conserved role in assembly of the ciliary motile apparatus. *PLoS*
868 *Genet* **10**, e1004577 (2014).
- 869 27. Seo, S. *et al.* BBS6, BBS10, and BBS12 form a complex with CCT/TRiC family chaperonins and
870 mediate BBSome assembly. *Proc Natl Acad Sci U S A* (2010).
- 871 28. Zhang, Q., Yu, D., Seo, S., Stone, E.M. & Sheffield, V.C. Intrinsic protein-protein interaction-
872 mediated and chaperonin-assisted sequential assembly of stable bardet-biedl syndrome protein
873 complex, the BBSome. *J Biol Chem* **287**, 20625-35 (2012).
- 874 29. Goetz, S.C., Liem, K.F., Jr. & Anderson, K.V. The spinocerebellar ataxia-associated gene Tau tubulin
875 kinase 2 controls the initiation of ciliogenesis. *Cell* **151**, 847-58 (2012).
- 876 30. Ye, X., Zeng, H., Ning, G., Reiter, J.F. & Liu, A. C2cd3 is critical for centriolar distal appendage
877 assembly and ciliary vesicle docking in mammals. *Proc Natl Acad Sci U S A* **111**, 2164-9 (2014).
- 878 31. Singla, V., Romaguera-Ros, M., Garcia-Verdugo, J.M. & Reiter, J.F. Ofd1, a human disease gene,
879 regulates the length and distal structure of centrioles. *Dev Cell* **18**, 410-24 (2010).
- 880 32. Joo, K. *et al.* CCDC41 is required for ciliary vesicle docking to the mother centriole. *Proc Natl Acad*
881 *Sci U S A* **110**, 5987-92 (2013).
- 882 33. Adler, P.N., Charlton, J. & Park, W.J. The Drosophila tissue polarity gene inturned functions prior to
883 wing hair morphogenesis in the regulation of hair polarity and number. *Genetics* **137**, 829-36.
884 (1994).
- 885 34. Collier, S. & Gubb, D. Drosophila tissue polarity requires the cell-autonomous activity of the fuzzy
886 gene, which encodes a novel transmembrane protein. *Development* **124**, 4029-37. (1997).
- 887 35. Collier, S., Lee, H., Burgess, R. & Adler, P. The WD40 repeat protein fritz links cytoskeletal planar
888 polarity to frizzled subcellular localization in the Drosophila epidermis. *Genetics* **169**, 2035-45
889 (2005).
- 890 36. Kim, S.K. *et al.* Planar Cell Polarity Acts Through Septins to Control Collective Cell Movement and
891 Ciliogenesis. *Science* **329**, 1337-1340 (2010).
- 892 37. Park, T.J., Haigo, S.L. & Wallingford, J.B. Ciliogenesis defects in embryos lacking inturned or fuzzy
893 function are associated with failure of planar cell polarity and Hedgehog signaling. *Nat Genet* **38**,
894 303-11 (2006).
- 895 38. Huttlin, E.L. *et al.* The BioPlex Network: A Systematic Exploration of the Human Interactome. *Cell*
896 **162**, 425-40 (2015).
- 897 39. Rual, J.F. *et al.* Towards a proteome-scale map of the human protein-protein interaction network.
898 *Nature* **437**, 1173-8 (2005).
- 899 40. Wang, Y., Yan, J., Lee, H., Lu, Q. & Adler, P.N. The proteins encoded by the Drosophila Planar
900 Polarity Effector genes inturned, fuzzy and fritz interact physically and can re-pattern the
901 accumulation of "upstream" Planar Cell Polarity proteins. *Dev Biol* (2014).
- 902 41. Gray, R.S. *et al.* The planar cell polarity effector Fuz is essential for targeted membrane trafficking,
903 ciliogenesis and mouse embryonic development. *Nat Cell Biol* **11**, 1225-32 (2009).
- 904 42. Alazami, A.M. *et al.* Molecular characterization of Joubert syndrome in Saudi Arabia. *Hum Mutat*
905 **33**, 1423-8 (2012).
- 906 43. Lopez, E. *et al.* C5orf42 is the major gene responsible for OFD syndrome type VI. *Hum Genet* **133**,
907 367-77 (2014).
- 908 44. Shaheen, R. *et al.* Genomic analysis of Meckel-Gruber syndrome in Arabs reveals marked genetic
909 heterogeneity and novel candidate genes. *Eur J Hum Genet* **21**, 762-8 (2013).
- 910 45. Srour, M. *et al.* Mutations in C5ORF42 cause Joubert syndrome in the French Canadian population.
911 *Am J Hum Genet* **90**, 693-700 (2012).
- 912 46. Damerla, R.R. *et al.* Novel Jbts17 mutant mouse model of Joubert syndrome with cilia transition
913 zone defects and cerebellar and other ciliopathy related anomalies. *Hum Mol Genet* (2015).
- 914 47. Brooks, E. & Wallingford, J.B. Control of vertebrate intraflagellar transport by the planar cell
915 polarity effector Fuz. *J. Cell Biol.* **198**, 37-45 (2012).
- 916 48. Brooks, E.R. & Wallingford, J.B. The Small GTPase Rsg1 is important for the cytoplasmic localization
917 and axonemal dynamics of intraflagellar transport proteins. *Cilia* **2**, 13 (2013).

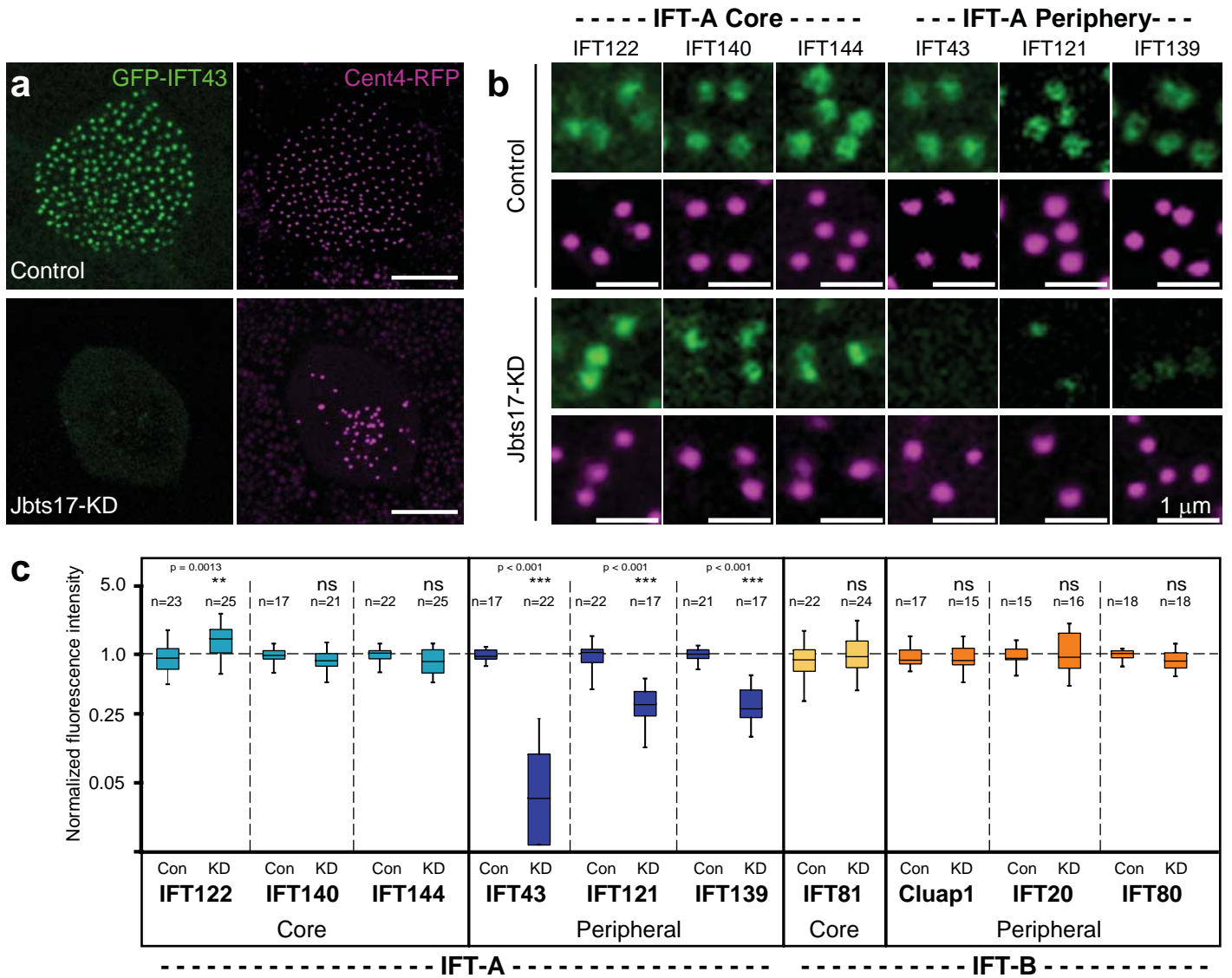
- 918 49. Gurrieri, F., Franco, B., Toriello, H. & Neri, G. Oral-facial-digital syndromes: review and diagnostic
919 guidelines. *Am J Med Genet A* **143A**, 3314-23 (2007).
- 920 50. Tabler, J.M. *et al.* Fuz mutant mice reveal shared mechanisms between ciliopathies and FGF-
921 related syndromes. *Dev Cell* **25**, 623-35 (2013).
- 922 51. Merrill, A.E. *et al.* Ciliary abnormalities due to defects in the retrograde transport protein
923 DYNC2H1 in short-rib polydactyly syndrome. *Am J Hum Genet* **84**, 542-9 (2009).
- 924 52. Mill, P. *et al.* Human and mouse mutations in WDR35 cause short-rib polydactyly syndromes due
925 to abnormal ciliogenesis. *Am J Hum Genet* **88**, 508-15 (2011).
- 926 53. Hsieh, Y.C. & Hou, J.W. Oral-facial-digital syndrome with Y-shaped fourth metacarpals and
927 endocardial cushion defect. *Am J Med Genet* **86**, 278-81 (1999).
- 928 54. Panigrahi, I., Das, R.R., Kulkarni, K.P. & Marwaha, R.K. Overlapping phenotypes in OFD type II and
929 OFD type VI: report of two cases. *Clin Dysmorphol* **22**, 109-14 (2013).
- 930 55. Saari, J., Lovell, M.A., Yu, H.C. & Bellus, G.A. Compound heterozygosity for a frame shift mutation
931 and a likely pathogenic sequence variant in the planar cell polarity-ciliogenesis gene WPCP in a
932 girl with polysyndactyly, coarctation of the aorta, and tongue hamartomas. *Am J Med Genet A*
933 (2014).
- 934 56. Li, Y. *et al.* Global genetic analysis in mice unveils central role for cilia in congenital heart disease.
935 *Nature* (2015).
- 936 57. Cui, C., Chatterjee, B., Lozito, T., Zhang, Z. & Lo, C.W. Wdpcp, a PCP Protein Required for
937 Ciliogenesis, Regulates Directional Cell Migration and Cell Polarity by Direct Modulation of the
938 Actin Cytoskeleton. *PLoS Biol.* **11**, e1001720 (2013).
- 939 58. Butler, M.T. & Wallingford, J.B. Control of vertebrate core planar cell polarity protein localization
940 and dynamics by Prickle 2. *Development* **142**, 3429-39 (2015).
- 941 59. Zilber, Y. *et al.* The PCP effector Fuzzy controls ciliary assembly and signaling by recruiting Rab8 and
942 Dishevelled to the primary cilium. *Mol Biol Cell* **24**, 555-65 (2013).
- 943 60. van Dam, T.J. *et al.* Evolution of modular intraflagellar transport from a coatomer-like progenitor.
944 *Proc Natl Acad Sci U S A* **110**, 6943-8 (2013).
- 945 61. Pan, X. *et al.* Mechanism of transport of IFT particles in *C. elegans* cilia by the concerted action of
946 kinesin-II and OSM-3 motors. *J Cell Biol* **174**, 1035-45 (2006).
- 947 62. Snow, J.J. *et al.* Two anterograde intraflagellar transport motors cooperate to build sensory cilia on
948 *C. elegans* neurons. *Nat Cell Biol* **6**, 1109-13 (2004).
- 949 63. Harris, J.A., Liu, Y., Yang, P., Kner, P. & Lehtreck, K.F. Single particle imaging reveals IFT-
950 independent transport and accumulation of EB1 in *Chlamydomonas* flagella. *Mol Biol Cell* (2015).
- 951 64. Seo, J.H. *et al.* Mutations in the planar cell polarity gene, Fuzzy, are associated with neural tube
952 defects in humans. *Hum Mol Genet* (2011).
- 953 65. Ooi, Y.S., Stiles, K.M., Liu, C.Y., Taylor, G.M. & Kielian, M. Genome-wide RNAi screen identifies
954 novel host proteins required for alphavirus entry. *PLoS Pathog* **9**, e1003835 (2013).
- 955 66. Moody, S.A. & Kline, M.J. Segregation of fate during cleavage of frog (*Xenopus laevis*) blastomeres.
956 *Anat Embryol (Berl)* **182**, 347-62 (1990).
- 957 67. Zeng, H., Hoover, A.N. & Liu, A. PCP effector gene *Inturned* is an important regulator of cilia
958 formation and embryonic development in mammals. *Dev Biol* **339**, 418-28 (2010).
- 959 68. Karpinka JB *et al.* Xenbase, the *Xenopus* model organism database; new virtualized system, data
960 types and genomes. *Nucleic Acids Res* **43**, D756-63 (2015).
- 961 69. Park, T.J., Mitchell, B.J., Abitua, P.B., Kintner, C. & Wallingford, J.B. Dishevelled controls apical
962 docking and planar polarization of basal bodies in ciliated epithelial cells. *Nat Genet* **40**, 871-9
963 (2008).
- 964 70. Lee, C.J., E.K., K., Gray, R.S., Park, T.J. & Wallingford, J.B. Whole-Mount Fluorescence
965 Immunocytochemistry on *Xenopus* Embryos. *Cold Spring Harbor Protocols* (2008).
- 966 71. Sive, H.L., Grainger, R.M. & Harland, R.M. Early Development of *Xenopus laevis*: A Laboratory
967 Manual. (2000).
- 968 72. Soding, J. Protein homology detection by HMM-HMM comparison. *Bioinformatics* **21**, 951-60
969 (2005).
- 970 73. Lobley, A., Sadowski, M.I. & Jones, D.T. pGenTHREADER and pDomTHREADER: new methods for
971 improved protein fold recognition and superfamily discrimination. *Bioinformatics* **25**, 1761-7

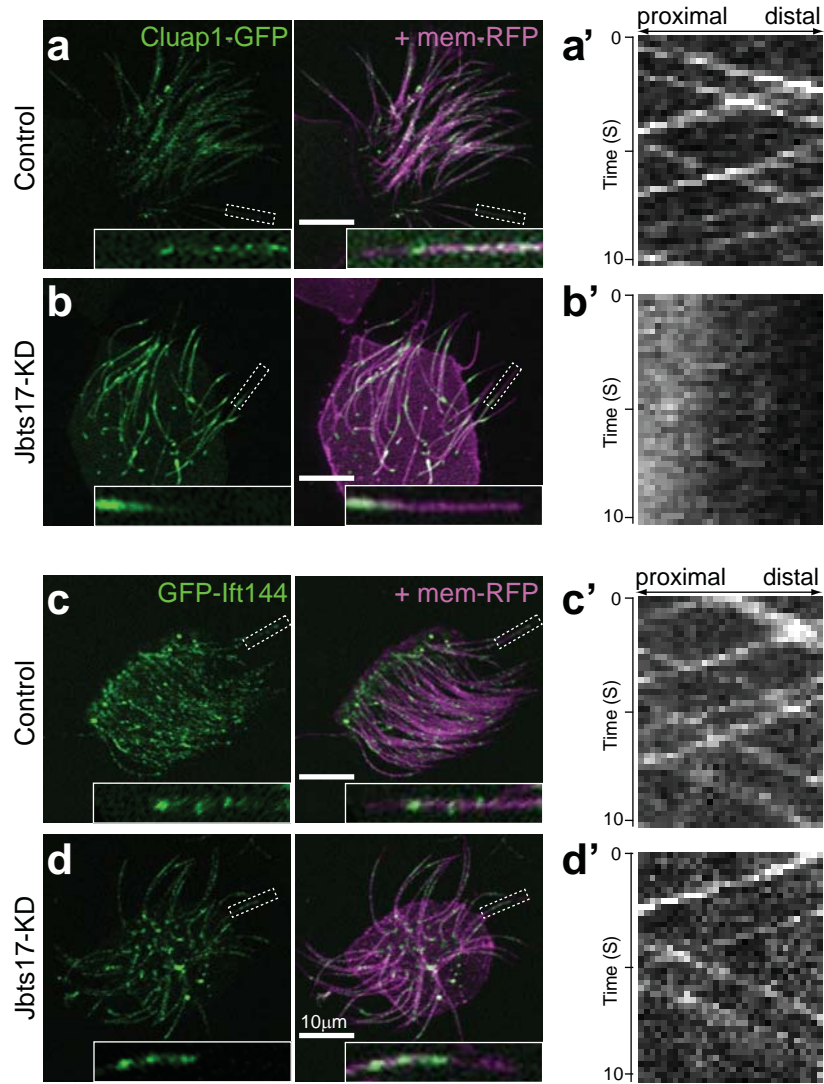
- 972 (2009).
973 74. Hasegawa, H. & Holm, L. Advances and pitfalls of protein structural alignment. *Curr Opin Struct*
974 *Biol* **19**, 341-8 (2009).
975



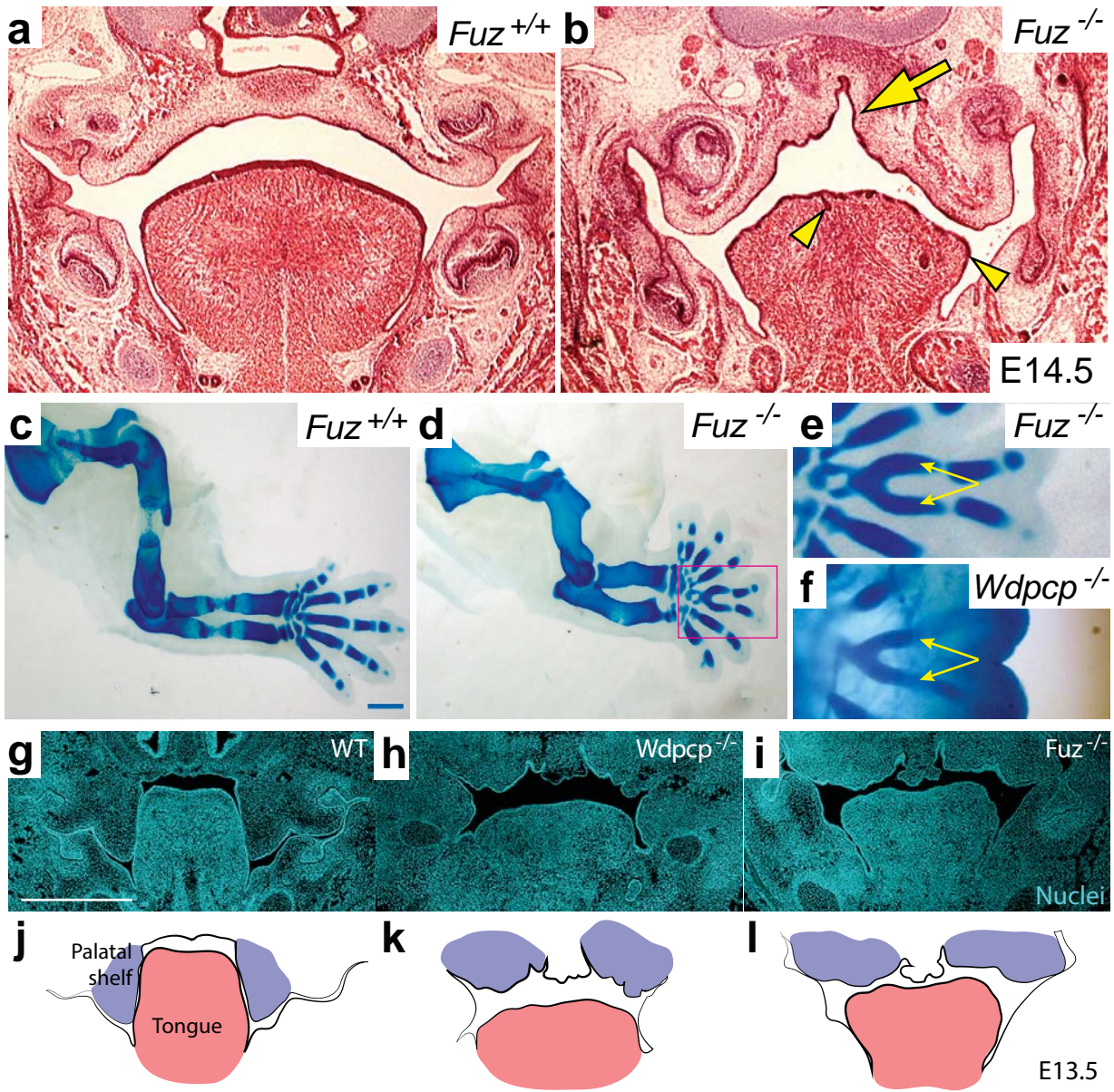
Toriyama et al. Figure 1



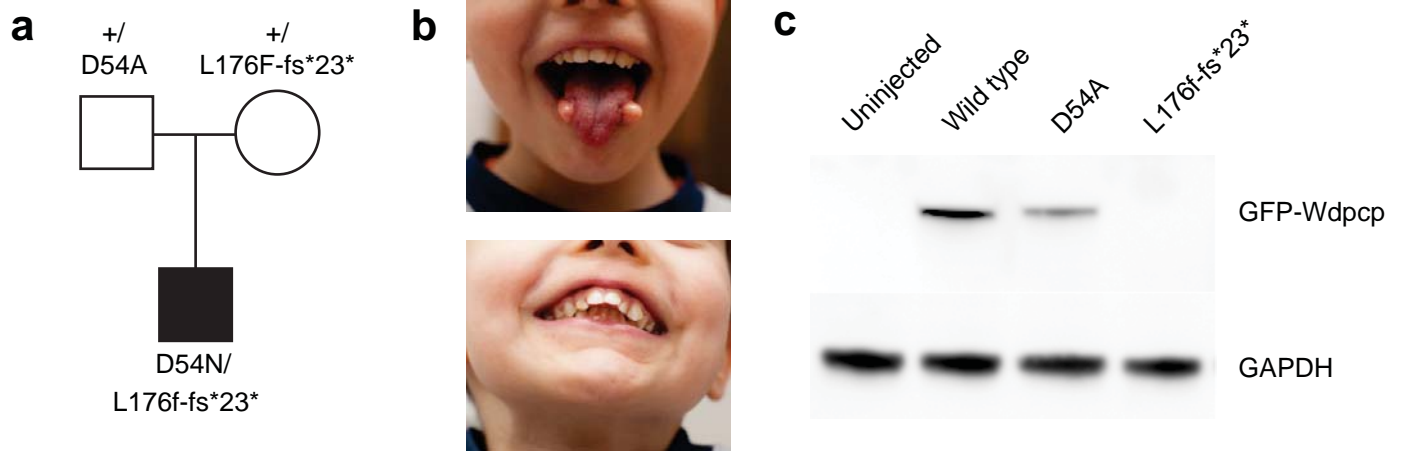




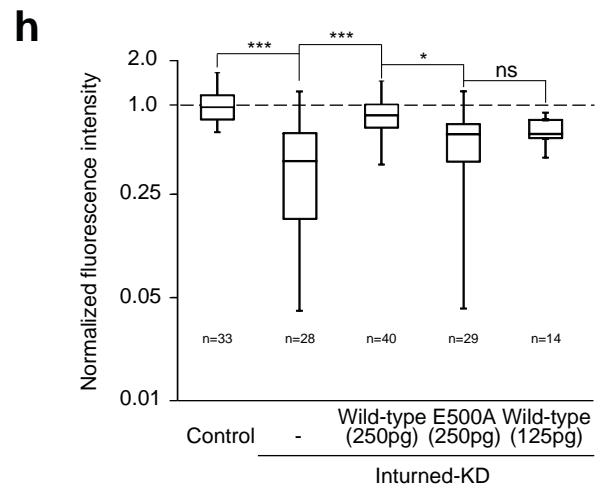
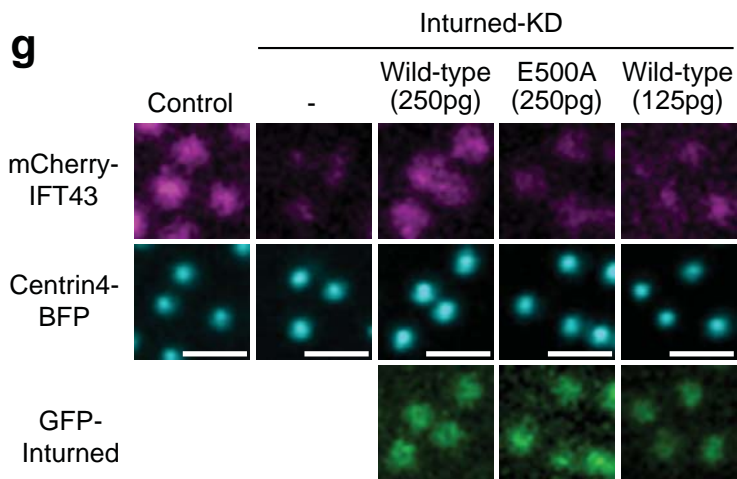
Toriyama et al. Figure 4

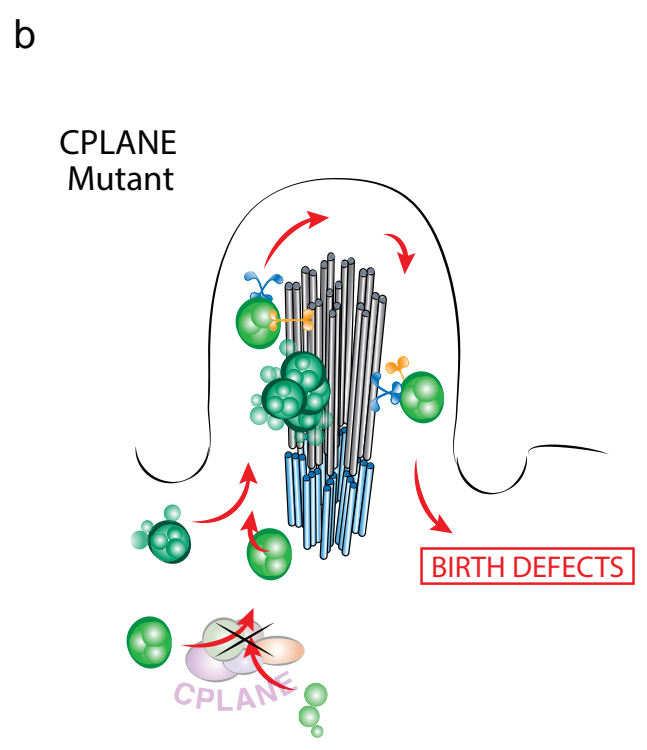
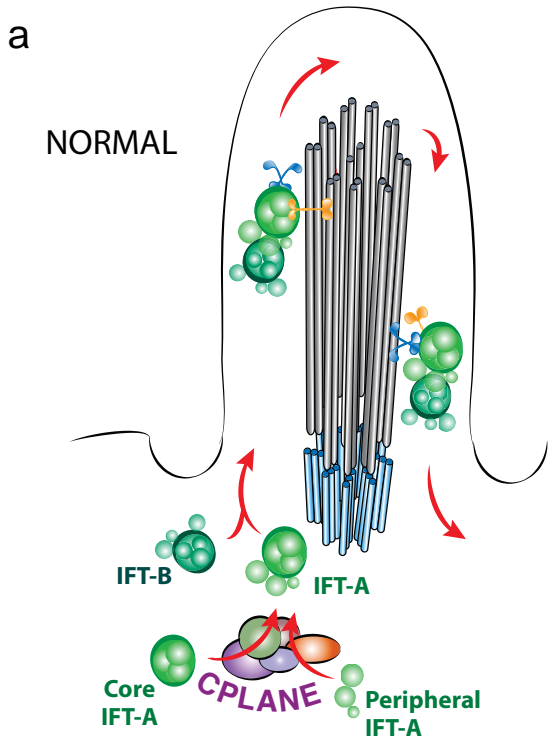


Oral-Facial-Digital - *WDPCP*



Short Rib Poydactyly - *INTU*





Toriyama et al., Figure 7